He *et al.*
Chinese Journal of Mechanical Engineering (2024) 37:79
https://doi.org/10.1186/s10033-024-01065-x

Chinese Journal of Mechanical Engineering

ORIGINAL ARTICLE

Open Access

Deployment Dynamic Modeling and Driving Schemes for a Ring-Truss Deployable Antenna

Baiyan He[1], Lijun Jia[1], Kangkang Li[1], Rui Nie[1*], Yesen Fan[2] and Guobiao Wang[1,3]

Abstract

Mesh reflector antennas are widely used in space tasks owing to their light weight, high surface accuracy, and large folding ratio. They are stowed during launch and then fully deployed in orbit to form a mesh reflector that transmits signals. Smooth deployment is essential for duty services; therefore, accurate and efficient dynamic modeling and analysis of the deployment process are essential. One major challenge is depicting time-varying resistance of the cable network and capturing the cable-truss coupling behavior during the deployment process. This paper proposes a general dynamic analysis methodology for cable-truss coupling. Considering the topological diversity and geometric nonlinearity, the cable network's equilibrium equation is derived, and an explicit expression of the time-varying tension of the boundary cables, which provides the main resistance in truss deployment, is obtained. The deployment dynamic model is established, which considers the coupling effect between the soft cables and deployable truss. The effects of the antenna's driving modes and parameters on the dynamic deployment performance were investigated. A scaled prototype was manufactured, and the deployment experiment was conducted to verify the accuracy of the proposed modeling method. The proposed methodology is suitable for general cable antennas with arbitrary topologies and parameters, providing theoretical guidance for the dynamic performance evaluation of antenna driving schemes.

Keywords Cable antenna, Deployment dynamics, Performance evaluation, Driving scheme, Deployable structure

1 Introduction

Spaceborne antennas have been widely used in various fields, such as space communications, military reconnaissance, and deep space exploration, as the essential equipment for transmitting and receiving signals [1–5]. In these applications, large spaceborne antennas are required to be stowed during launch and then fully deployed after entering the desired orbit. Deployable antennas have received more attention and development, along with the acceleration of human exploration of outer space [6–11]. Cable antennas are currently the focus of mainstream research owing to their high surface accuracy, structural simplicity, and stowage efficiency [12–16]. Take the ring-truss mesh reflector antenna as an example. It consists of five parts: the ring truss, front cable net, rear cable net, tension ties, and metal mesh, as shown in Figure 1 [17–19]. The truss of the antenna contains several parallelogram units composed of the transverse bar, longitudinal bar, thick oblique bar, thin oblique bar, five-dimensional hinge, three-dimensional hinge, and pulley. Figure 1 describes the driving mode of the ring-truss mesh reflector antenna, which is deployed using motors to contract the driving ropes in the oblique bars or by the torsion springs in the connecting hinges of the parallelogram units [20–23]. The three-dimensional hinge is equipped with synchronization gears so that each unit can be deployed synchronously. The challenges of ensuring the smooth and successful deployment of

*Correspondence:
Rui Nie
nierui@tju.edu.cn
[1] Key Laboratory of Mechanism Theory and Equipment Design, Ministry of Education, Tianjin University, Tianjin 300350, China
[2] Xi'an Institute of Space Radio Technology, Xi'an 710000, China
[3] International Institute for Innovative Design and Intelligent Manufacturing of Tianjin University in Zhejiang, Shaoxing 312077, China

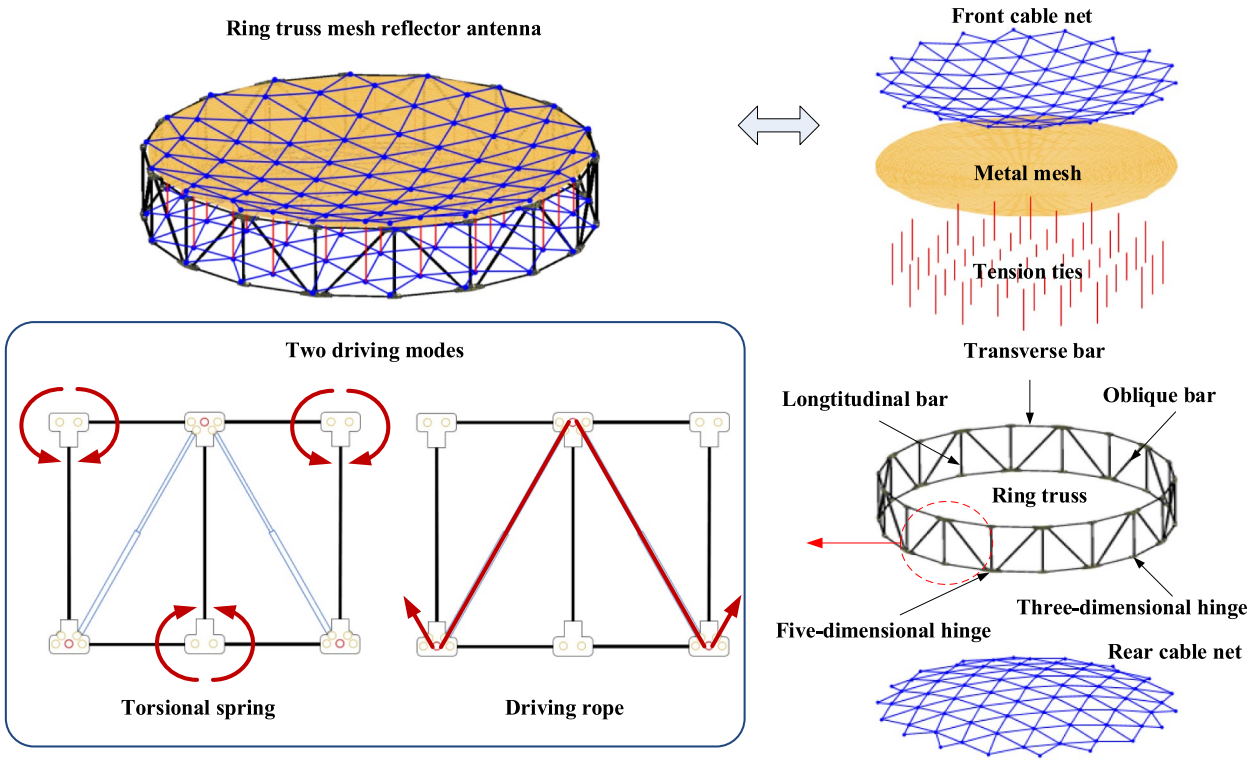

Figure 1 Ring-truss mesh reflector antenna

the antenna focus on accurately capturing the dynamic behavior of the antenna and revealing the influence of driving parameters on the dynamic performance. The key to solving this problem is the dynamic modeling and analysis of the cable-truss coupling effect during deployment.

The boundary nodes of the cable network are connected to the truss, which stretches the cable network to unfold by connecting nodes [24–28]. In this process, each cable constantly switches between the slacked and tensioned states. The cables interact with each other, resulting in time-varying cable tensions and geometric configurations. The resistance applied to the truss by the boundary cables also varies during deployment [29–33]. The influence of the cable network on the deployment of the truss should be fully captured in the cable-truss coupling dynamic analysis. Nevertheless, the strong geometric nonlinearity and superposition of the small deformation of cables on their significant motion lead to the modeling and solution of problems [34–37]. In addition, the cable network topology, truss configuration, and antenna parameters vary with applications, challenging the generality [38–43]. Therefore, a general and stable modeling and analysis method for cable truss mechanisms applicable to various cable antennas is urgently required.

The cable network contains a large number of cables whose tension varies with time during deployment. Many scholars have studied the deployment process of the cable network [44–48]. Greco et al. [49] modeled cable segments using catenary elements. Nie et al. [50] used a spring-damper element to establish the cable network model. Ambrosio et al. [51] studied the optimal deployment of a radar antenna using the finite element method. He et al. [20] proposed a general deployment analysis method for soft cable networks, ranging from slacked to tensioned. However, these studies used numerical solution algorithms based on time discretization, and the time-varying tensions of the boundary cables during deployment were not derived.

Researchers have also studied the coupling effects between cable networks and trusses [52–56]. Zhang et al. [57] established a mapping relationship among the antenna structure, deployment trajectory, and control system. Lu et al. [58] modeled the cable wheel system of an antenna by considering the long-distance force transmission. Jiang et al. [59] established a dynamic model of a ring-truss antenna using an absolute nodal coordinate formulation. Nie et al. [60] established a truss deployment model using the Lagrange equation. Although the above studies realized the integrated calculation of the truss and cable network by numerical algorithm, an

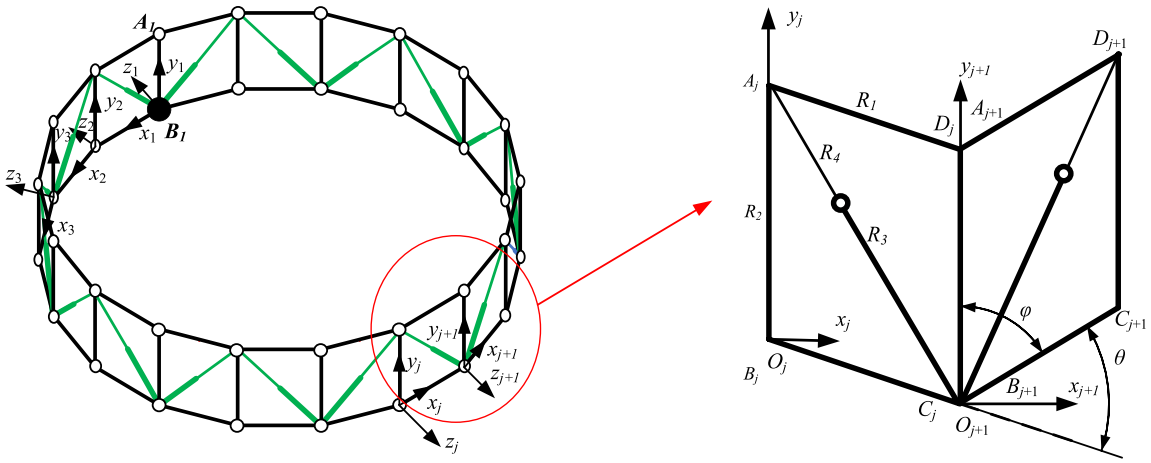

Figure 2 The ring truss and the parallelogram unit

analytical method capturing the cable-truss coupling effects and applied to various cable-truss antennas has not been well studied.

Many scholars have extensively researched antenna deployable mechanism designs, deployment kinematics, and dynamic analyses. Meng et al. [61] proposed a deployable truss configuration with good dynamic performance. Wu et al. [62] derived the governing equations for the deployment motion and boundary conditions. Wang et al. [63] designed a deployment experiment to investigate the antenna deployment process. Liu et al. [64] developed a novel equivalent dynamic model for vibration analysis. However, the existing research focuses on the dynamic analysis of the deployment process. There are no driving modes and parameter design approaches aimed at dynamic performance.

In summary, there are still no general and effective analytical models for the deployment analysis of cable-truss coupling mechanisms, leading to problems in dynamic performance optimization and driving design. In this study, we propose a parameterized cable-truss integrated deployment analysis method by introducing the graph theory to depict the topology of the cable network and truss. A scaled prototype was manufactured, and a deployment experiment was conducted to verify the accuracy of the proposed dynamic analysis method. The driving parameters are designed based on the required driving force and energies. The influence of the driving mode and parameters on the dynamic behavior of the antenna were thoroughly studied and discussed to provide theoretical guidance to improve the dynamic performance of ring-truss deployable antennas.

2 Kinematic Analysis of the Truss

In this section, we take the ring truss as an example to analyze its deployment motion, which provides fundamental variables for the dynamic modeling of cable-truss coupling. As shown in Figure 2, the ring truss is composed of several similar parallelogram units consisting of bars and hinges. The truss expands from a fully stowed state to a deployed state by contracting the oblique bar. The acute angle between the transverse and longitudinal bars is defined as the deployment angle ϕ that represents the antenna's deployment phase, which varies from 0 to π/2 rad. In Figure 2, A_j, B_j, C_j, and D_j denote the truss nodes in parallelogram unit j. C_j and D_j coincide with A_{j+1} and B_{j+1} of parallelogram unit (j+1). R_1, R_2, R_3, and R_4 denote the lengths of the transverse, longitudinal, thick oblique, and thin oblique bars, respectively. The acute angle between the two adjacent units is defined as $\theta = 2\pi/n$, where n is the number of parallelogram units ($n \geq 4$, and n is an even number).

As shown in Figure 2, A_1B_1 is considered as the fixed bar, and the frame (x_j, y_j, z_j) is taken as the local coordinate system of parallelogram unit j. The local coordinate system of the first parallelogram unit is chosen as the global coordinate system. If the position vector of an arbitrary point P in parallelogram unit j under the local coordinate system (x_j, y_j, z_j) is $\boldsymbol{r}_P^j$, its position vector under the local coordinate system (x_i, y_i, z_i) is derived as

$$\boldsymbol{r}_P^i = \boldsymbol{T}^{ij}\boldsymbol{r}_P^j, \tag{1}$$

$$\boldsymbol{T}^{ij}=\begin{bmatrix}\cos\left[(j-i)\theta\right] & 0 & \sin\left[(j-i)\theta\right] & \left\{\sum_{k=i+1}^{j}\cos\left[(k-i-1)\theta\right]\right\}R_1\sin\varphi\\ 0 & 1 & 0 & \frac{1}{2}\left[1-(-1)^{j-1}\right]R_1\cos\varphi\\ -\sin\left[(j-i)\theta\right] & 0 & \cos\left[(j-i)\theta\right] & \left\{-\sum_{k=i+1}^{j}\sin\left[(k-i-1)\theta\right]\right\}R_1\sin\varphi\\ 0 & 0 & 0 & 1\end{bmatrix}, \tag{2}$$

where $\boldsymbol{T}^{ij}$ is the coordinate transformation matrix.

The velocity vector of the truss node is obtained by taking the derivative of the position vector. Assuming that the velocity vector of an arbitrary point in parallelogram unit j under the local coordinate system (x_j, y_j, z_j) is $\boldsymbol{r}_P^{j'}$, its velocity vector under the local coordinate system (x_i, y_i, z_i) is denoted by

$$\boldsymbol{r}_P^{i'}=\boldsymbol{T}^{ij'}\boldsymbol{r}_P^{j}+\boldsymbol{T}^{ij}\boldsymbol{r}_P^{j'}, \tag{3}$$

The position vectors of nodes A_j, B_j, C_j, and D_j in the local coordinate system are derived as

$$\begin{cases}\boldsymbol{r}_{A_j}^{j}=\left[\,0\;0\;\mathrm{R}_2\;1\,\right]^{\mathrm{T}},\ \boldsymbol{r}_{C_j}^{1}=\boldsymbol{r}_{B_{j+1}}^{1},\\ \boldsymbol{r}_{B_j}^{j}=\left[\,0\;0\;0\;1\,\right]^{\mathrm{T}},\ \boldsymbol{r}_{D_j}^{1}=\boldsymbol{r}_{A_{j+1}}^{1},\end{cases} \tag{4}$$

In this way, the position and velocity vectors of the truss nodes obtained in the global coordinate can be obtained. Assuming that the mass of the bars was evenly distributed along the length direction, their centroids were the geometric centers. The position vectors of the centroids are denoted by the average position vectors of the endpoints, as shown in Eq. (5).

$$\begin{cases}\boldsymbol{r}_{A_jB_j}^{1}=\dfrac{\boldsymbol{r}_{A_j}^{1}+\boldsymbol{r}_{B_j}^{1}}{2},\ \boldsymbol{r}_{B_jC_j}^{1}=\dfrac{\boldsymbol{r}_{B_j}^{1}+\boldsymbol{r}_{C_j}^{1}}{2},\\ \boldsymbol{r}_{C_jD_j}^{1}=\dfrac{\boldsymbol{r}_{C_j}^{1}+\boldsymbol{r}_{D_j}^{1}}{2},\ \boldsymbol{r}_{D_jA_j}^{1}=\dfrac{\boldsymbol{r}_{D_j}^{1}+\boldsymbol{r}_{A_j}^{1}}{2},\\ \boldsymbol{r}_{A_jC_j}^{1}=\boldsymbol{r}_{A_j}^{1}+\\ \dfrac{m_4\frac{1}{2}R_4+m_3\left(\sqrt{R_1^2+R_2^2+2R_1R_2\cos\varphi}-\frac{1}{2}R_3\right)}{(m_3+m_4)\sqrt{R_1^2+R_2^2+2R_1R_2\cos\varphi}}\left(\boldsymbol{r}_{C_j}^{1}-\boldsymbol{r}_{A_j}^{1}\right),\\ \boldsymbol{r}_{B_jD_j}^{1}=\boldsymbol{r}_{B_j}^{1}+\\ \dfrac{m_3\frac{1}{2}R_3+m_4\left(\sqrt{R_1^2+R_2^2+2R_1R_2\cos\varphi}-\frac{1}{2}R_4\right)}{(m_3+m_4)\sqrt{R_1^2+R_2^2+2R_1R_2\cos\varphi}}\left(\boldsymbol{r}_{D_j}^{1}-\boldsymbol{r}_{B_j}^{1}\right),\end{cases} \tag{5}$$

where m_3 and m_4 are the mass of the thick and thin oblique bars, respectively.

Similarly, the centroid velocity and rotational angular velocity of the bars are denoted by

$$\begin{cases}\boldsymbol{v}_{A_jB_j}^{1}=\dfrac{\dot{\boldsymbol{r}}_{A_j}^{1}+\dot{\boldsymbol{r}}_{B_j}^{1}}{2},\boldsymbol{v}_{B_jC_j}^{1}=\dfrac{\dot{\boldsymbol{r}}_{B_j}^{1}+\dot{\boldsymbol{r}}_{C_j}^{1}}{2},\boldsymbol{v}_{C_jD_j}^{1}=\dfrac{\dot{\boldsymbol{r}}_{C_j}^{1}+\dot{\boldsymbol{r}}_{D_j}^{1}}{2}\\ \boldsymbol{v}_{D_jA_j}^{1}=\dfrac{\dot{\boldsymbol{r}}_{D_j}^{1}+\dot{\boldsymbol{r}}_{A_j}^{1}}{2},\\ \boldsymbol{v}_{A_jC_j}^{1}=\dot{\boldsymbol{r}}_{A_j}^{1}+\dfrac{m_4\frac{1}{2}R_4+m_3\left(L-\frac{1}{2}R_3\right)}{(m_3+m_4)L}\left(\dot{\mathbf{r}}_{C_j}^{1}-\dot{\mathbf{r}}_{A_j}^{1}\right),\\ \boldsymbol{v}_{B_jD_j}^{1}=\dot{\boldsymbol{r}}_{B_j}^{1}+\dfrac{m_3\frac{1}{2}R_3+m_4\left(L-\frac{1}{2}R_4\right)}{(m_3+m_4)L}\left(\dot{\boldsymbol{r}}_{D_j}^{1}-\dot{\boldsymbol{r}}_{B_j}^{1}\right),\\ \boldsymbol{\omega}_{A_jB_j}^{1}=\dfrac{\dot{\boldsymbol{r}}_{A_j}^{1}-\dot{\boldsymbol{r}}_{B_j}^{1}}{R_2},\boldsymbol{\omega}_{B_jC_j}^{1}=\dfrac{\dot{\mathbf{r}}_{C_j}^{1}-\dot{\boldsymbol{r}}_{B_j}^{1}}{R_1},\boldsymbol{\omega}_{C_jD_j}^{0}=\dfrac{\dot{\boldsymbol{r}}_{D_j}^{1}-\dot{\boldsymbol{r}}_{C_j}^{1}}{R_2},\\ \boldsymbol{\omega}_{D_jA_j}^{0}=\dfrac{\dot{\boldsymbol{r}}_{D_j}^{1}-\dot{\boldsymbol{r}}_{A_j}^{1}}{R_1},\boldsymbol{\omega}_{A_jC_j}^{1}=\dfrac{\dot{\boldsymbol{r}}_{C_j}^{1}-\dot{\boldsymbol{r}}_{A_j}^{1}}{L},\boldsymbol{\omega}_{B_jD_j}^{1}=\dfrac{\dot{\boldsymbol{r}}_{D_j}^{1}-\dot{\boldsymbol{r}}_{B_j}^{1}}{L},\end{cases} \tag{6}$$

where L is the length of drive rope in the parallelogram unit.

According to the above derivation, we obtained the displacement, velocity, and angular velocity of the bars and hinges in the global coordinate under the arbitrary deployment angle. The deployment process of the truss was accurately depicted.

3 Cable-Truss Coupling Dynamic Analysis Method

In the deployment of the cable antenna, the complex motion of the truss, geometric nonlinearity, time-varying resistance, and cable-truss real-time coupling effect significantly influenced the dynamic performance. This section introduces a cable-truss coupling dynamic analysis method to accurately capture the dynamic behavior of the antenna during deployment. The cable network was discretized into many cable elements according to its topological connection. Parameterized equilibrium equations were derived by depicting the connection of the cables with a topology matrix. In this way, the explicit expression of the time-varying tension of the boundary cables was derived, which can be coupled with the truss model. Then, we derived the expressions of the kinetic and gravitational potential energy of the truss based on the kinematic analysis in Section 2, and established the

dynamic model of the cable antenna using the Lagrange equation of the first kind.

3.1 The Cable Network Modeling

During the antenna's deployment, each cable switches between the slacked and tensioned states under the stretching of the truss. The cables interact with each other during the unfolding process, resulting in time-varying cable tensions and geometric shapes. Additionally, the cables' small deformations are coupled with their large-scale overall motion, along with the cable's strong geometric nonlinearity, leading to problems in the derivation of the time-varying tensions of the boundary cables, which are also the resistance load of the truss.

Figure 3 shows the cable network. The cable nodes connected to the truss are defined as boundary nodes, while the other cable nodes are free nodes. The cables connected to the truss are defined as boundary cables, while the other cables are inner cables. The constitutive model of the cable element adopts Hooke's law with variable stiffness, which depends on the slacked and tensioned states of the cable element. When the distance between the two end nodes of the cable element is larger than the cable's unstressed length, the cable is in a tensioned state, and the stiffness is calculated using the geometric parameters and elastic modulus. Once the distance between the two endpoints of the cable element was less than or equal to the unstressed length of the cable, the cable was slaked, and the stiffness was set to zero. In this way, all the constitutive equations of the cable element can be derived to form systematic equilibrium equations at arbitrary moments of the unfolding process. In the following derivation, the connection of the cable elements and cable nodes is depicted by the topology matrix so that the systematic equilibrium equations of the cable network can be parameterized for application to various topologies and parameters. Based on cable network modeling, we derived the explicit expression for the time-varying tension of boundary cables.

Assuming that the cable network consists of m cable elements and n cable nodes with n_{f} free nodes and n_{b} boundary nodes, number these cables and nodes in any order and the corresponding topology matrix are obtained by Eq. (7). Suppose that cable i connects nodes j_{a} and j_{b} ($j_{\mathrm{a}} \le j_{\mathrm{b}}$), then set the j_{a}th and j_{b}th elements of the ith row of the topology matrix $\boldsymbol{D}$ to 1 and -1, and set other elements in the matrix to zero. Taking the simplified cable network in Figure 4(a) as an example, the black numbers represent the nodal labels, and the numbers inside the red circles represent the cable labels. Figure 4(b) shows the corresponding topology matrix of the cable network in Figure 4(a) according to Eq. (7).

$$\boldsymbol{D}(i,j) = \begin{cases} 1, & j = j_{\mathrm{a}}, \\ -1, & j = j_{\mathrm{b}}, \\ 0, & \text{others}. \end{cases} \tag{7}$$

The topology matrix is used to describe the cable network and truss in this study. Therefore, the matrix operation can be used to solve the nonlinear equations, and its stability and computational efficiency are excellent.

The mass of the cable network is evenly distributed at the corresponding nodes, and the external forces applied to the free nodes during unfolding are always equal to the gravity of the equivalent node. Thus, the equilibrium equations of the free nodes at an arbitrary moment can be expressed as

$$-\boldsymbol{D}_{\mathrm{f}}^{\mathrm{T}} \operatorname{diag}\{\boldsymbol{Q}(t)\emptyset\boldsymbol{L}(t)\}\boldsymbol{D}_{\mathrm{f}}\boldsymbol{S}_{\mathrm{f}}(t) = \boldsymbol{G}_{\mathrm{f}}, \tag{8}$$

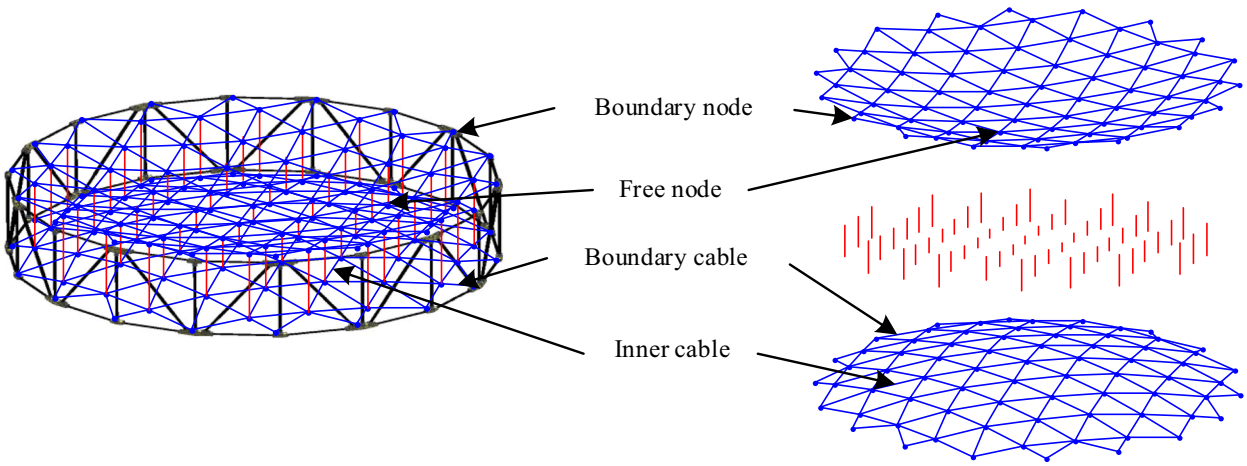

Figure 3 The cable network of cable antennas

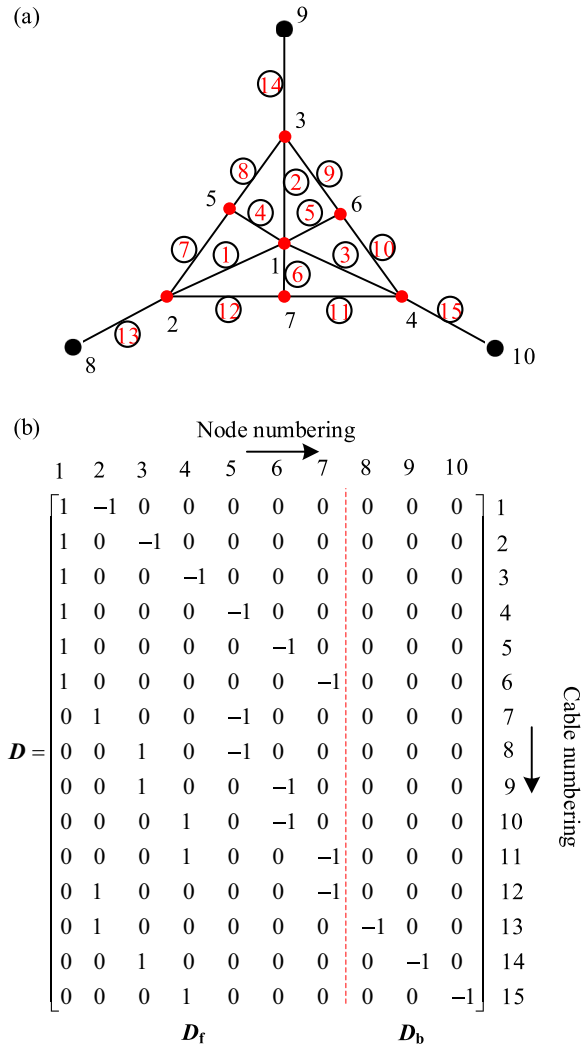

Figure 4 A simplified cable network with 10 nodes and 15 cables. **a** Serial number of cable elements and cable nodes. **b** The cable network's topological matrix

where $\boldsymbol{Q}(t)$ is the cable tension vector at time t; $\boldsymbol{L}(t)$ is the tensile length vector of the a cables at time t; $\boldsymbol{S}_{\mathrm{f}}(t)$ is the coordinate matrix of the free nodes at time t; and $\boldsymbol{G}_{\mathrm{f}}$ is the n_{f}×3-dimensional equivalent gravity matrix, whose elements are the equivalent gravity at each node.

The cable tension vector $\boldsymbol{Q}(t)$ is

$$\boldsymbol{Q}(t) = \boldsymbol{K}(t) \circ \boldsymbol{\delta l}(t), \tag{9}$$

where ∘ is the Hadamard product, which represents the product of the elements of the corresponding positions of the two matrices, and

$$\boldsymbol{K}(t) = \left[k_1(t)\ k_2(t)\ \cdots\ k_i(t)\ \cdots\ k_m(t) \right], \tag{10}$$

$$k_i(t) = \begin{cases} k_i,\ l_i(t) > l_i, \\ 0,\ l_i(t) \le l_i, \end{cases} \tag{11}$$

$$\boldsymbol{\delta l}(t) = \left[\delta l_1(t)\ \delta l_2(t)\ \cdots\ \delta l_i(t)\ \cdots\ \delta l_m(t) \right], \tag{12}$$

$$\delta l_i(t) = \begin{cases} (l_i(t) - l_i), & l_i(t) > l_i, \\ 0, & l_i(t) \le l_i, \end{cases} \tag{13}$$

where $\boldsymbol{K}$(t) is the cable stiffness vector at time t; $\boldsymbol{\delta l}(t)$ is the cable elongation vector at time t; k_i is the linearized stiffness of cable i; l_i is the unstressed length of cable i; and l_i(t) is the tensile length of the cable at time t, which is the element in the tensile length vector of the cables shown in Eq. (14).

$$\boldsymbol{L}(t) = \sqrt{[\boldsymbol{DX}(t)]^2 + [\boldsymbol{DY}(t)]^2 + [\boldsymbol{DZ}(t)]^2}. \tag{14}$$

Up to now, coordinates of the free nodes can be calculated by substituting Eqs. (9) and (14) into Eq. (8), and the coordinates of the boundary nodes are equal to the corresponding coordinates of the truss nodes derived in Section 2.

According to the derivation above, we can obtain the explicit expression for the time-varying tension of the boundary cables using Eq. (15). The real-time coupling effect between the soft cables and truss was reflected by the time-varying boundary cable tension and boundary node coordinates.

$$\begin{aligned} &\left[\boldsymbol{F}_{\mathrm{A}}\ ;\boldsymbol{F}_{\mathrm{B}} \right] = \\ &\left[-\boldsymbol{D}_{\mathrm{b}}^{\mathrm{T}} \mathrm{diag}\{\boldsymbol{Q}(t)\emptyset\boldsymbol{L}(t)\}\boldsymbol{D}_{\mathrm{b}}\boldsymbol{S}_{\mathrm{d}}(t)\ \boldsymbol{0}_{n_{\mathrm{b}}\times 1} \right], \end{aligned} \tag{15}$$

where $\boldsymbol{S}_{\mathrm{d}}(t)$ is the coordinate matrix of the boundary nodes at time t.

The elastic energy of the cable network can be denoted by

$$V_{\mathrm{c}}(t) = \frac{1}{2}\boldsymbol{Q}(t)\boldsymbol{\delta l}(t)^{\mathrm{T}}. \tag{16}$$

3.2 The Truss Modeling

During deployment, the generalized driving force and resistance load of the boundary cables lead to variations in the energy of the truss, including the kinetic energy, gravitational potential energy, and systematic dissipation energy. The kinetic energy of the truss consists of the kinetic energies of the bars and hinges, as shown in Eq. (17). Assuming that the mass of the bars is evenly distributed along the length direction, their mass is concentrated in the centroids. The kinetic energy of the bars is denoted by Eq. (18). The kinetic energy of the hinges is expressed by Eq. (19).

$$T = T_{\mathrm{b}} + T_{\mathrm{h}}, \tag{17}$$

$$\begin{aligned} T_{\mathrm{b}} = \frac{1}{2}\sum_{j=1}^{n}\Bigg[& m_1\left(\left|\boldsymbol{v}_{A_jD_j}\right|^2 + \left|\boldsymbol{v}_{B_jC_j}\right|^2\right) + m_2\left|\boldsymbol{v}_{A_jB_j}\right|^2 \\ & + (m_3+m_4)\left(\left|\boldsymbol{v}_{A_jC_j}\right|^2 + \left|\boldsymbol{v}_{B_jD_j}\right|^2\right) \\ & + J_1\left(\left|\boldsymbol{\omega}_{A_jD_j}\right|^2 + \left|\boldsymbol{\omega}_{B_jC_j}\right|^2\right) + J_2\left|\boldsymbol{\omega}_{A_jB_j}\right|^2 \\ & + J_3\left|\boldsymbol{\omega}_{A_jC_j}\right|^2 + J_4\left|\boldsymbol{\omega}_{B_jD_j}\right|^2\Bigg], \end{aligned} \tag{18}$$

$$T_{\mathrm{h}} = \frac{1}{2}\sum_{j=1}^{n}\left(m_{\mathrm{t}}\left|\boldsymbol{v}^1_{\mathrm{A_j}}\right|^2 + m_{\mathrm{f}}\left|\boldsymbol{v}^1_{\mathrm{B_j}}\right|^2\right), \tag{19}$$

where T_{b} and T_{h} denote the kinetic energies of the bars and hinges, respectively. m_1 and m_2 are the masses of the transverse and longitudinal bars, respectively. J_1, J_2, J_3, and J_4 denote the rotational inertia of the transverse, longitudinal, odd unit oblique, and even unit oblique bars, respectively, and were calculated by Eq. (20). m_{t} and m_{f} are the masses of the three-dimensional and five-dimensional hinges, respectively.

$$\begin{cases} J_1 = \frac{1}{3}m_1R_1^2,\ J_3 = \frac{1}{3}m_3R_3^2 + \frac{1}{12}m_4R_4^2 + m_4\left(L - \frac{R_4}{2}\right)^2, \\ J_2 = \frac{1}{3}m_2R_2^2,\ J_4 = \frac{1}{3}m_4R_4^2 + \frac{1}{12}m_3R_3^2 + m_3\left(L - \frac{R_3}{2}\right)^2, \end{cases} \tag{20}$$

Except for the kinematic energy variation, the centroid of the antenna varied during deployment, which leads to gravitational potential energy variation. The fully deployed state of the antenna is defined as the reference configuration for zero gravitational potential energy. Then, gravitational potential energy of the truss, including the potential energies of the bars and hinges, is shown in Eq. (21).

$$G = \left[\frac{n}{2}(m_2 + m_{\mathrm{t}} + m_{\mathrm{f}} + m_3 + m_4) + nm_1\right]gR_1\cos\varphi, \tag{21}$$

where g is the gravitational acceleration, and g is set according to the working conditions.

The antenna deployment process is relatively slow, and the damping of the hinges can be considered viscous damping proportional to the deployment angular velocity. According to the Rayleigh dissipation formula, the systematic dissipation energy can be expressed as

$$\Phi = \sum_{j=1}^{n} 4\int_0^{\nu} \xi\varphi' d\varphi' = 2n\xi\varphi'^2, \tag{22}$$

where ξ represents the dissipation coefficient.

If the antenna is driven by the torsion springs in the three-dimensional hinge, the angular variation of the torsion springs corresponds to the angular displacement during deployment, and their generalized driving torques are denoted by Eq. (23). If the antenna is deployed by the driving rope in the oblique bars, then the length variation of the driving rope corresponds to the telescopic length variation of the oblique bars. The generalized driving torque is given by Eq. (24).

$$M_{\mathrm{s}} = nk_{\mathrm{s}}(\varphi_{\mathrm{d}} - \varphi) - \kappa\varphi', \tag{23}$$

$$M_{\mathrm{r}} = F_{\mathrm{r}}\frac{\partial L}{\partial \varphi}, \tag{24}$$

where M_{s} and M_{r} denote the generalized driving torque of the torsion springs and driving rope; k_s, ϕ_{d}, and κ are the torsion spring's stiffness coefficient, initial pre-deflection angle, and damping coefficient, respectively; and F_{r} is the driving force of the driving rope.

3.3 Cable-Truss Coupling Dynamic Modeling

The cable-truss coupling dynamic model is established by the Lagrange equation of the first kind in this section. The deployment angle ϕ is chosen as the generalized coordinate. During deployment, the kinetic and potential energies of the truss as well as the dissipation energy are derived, which are always equal to the work done by the driving torque and resistance load applied to the cable-truss connecting nodes, as shown in Eq. (25). The time-varying tension of the boundary cables applied to the connecting nodes on the truss is derived in Section 3.1, while the energy variation of the truss is modeled in Section 3.2. In summary, the cable-truss coupling dynamic model is established by substituting Eqs. (15), (17), and (21)–(24) into Eq. (25), and the real-time coupling of the interaction forces and positional constraints between the cable network and truss in the deployment are fully captured.

$$\frac{d}{\mathrm{d}t}\frac{\partial T}{\partial \varphi'} - \frac{\partial T}{\partial \varphi} + \frac{\partial G}{\partial \varphi} + \frac{\partial \Phi}{\partial \varphi'} = M + \sum_{j=1}^{n}\left(\boldsymbol{F}_{A_j}\frac{\partial \boldsymbol{r}_{A_j}}{\partial \varphi} + \boldsymbol{F}_{B_j}\frac{\partial \boldsymbol{r}_{B_j}}{\partial \varphi}\right), \tag{25}$$

where T denotes the kinetic energy of the truss; G denotes the gravitational potential energy of the truss; Φ denotes the systematic dissipation energy; M denotes the generalized driving torque; and F_{Aj} and F_{Bj} denote the tension vector of the 1×4-dimensional boundary cables applied to the nodes A_j and B_j of the jth parallelogram unit.

4 Comparison and Experimental Verification

This section verifies the proposed dynamic modeling and analysis method based on literature and experiments. The calculated results were compared with the previous literature and experimental data.

4.1 Comparison with Other Literature

A similar simulation was conducted for comparison with previous literature to verify the modelling method used in this study. Figure 5 shows the antenna configuration and cable network serial numbers used in the simulation. We calculated the required driving force under the desired deployment motion in Ref. [60]. The results are shown in Figures 6, 7 and 8. These results were compared with those in Ref. [60]. The antenna parameters are listed in Table 1. The unstressed cable lengths are listed in Table 2.

Assume the antenna is deployed in a predesigned deployment motion, whose deployment angle and angular velocity curves are shown in Figure 6. The deployment time was set to 10000 s, mainly for comparison with the calculation results in Ref. [50] to verify the accuracy of the modeling method. The deployment angular velocity gradually increased and then decreased to zero before locking, which could effectively avoid impact and vibration to achieve the desired smooth deployment.

We calculated the time-varying tension of the cable network under the predesigned deployment motion in Figure 6. Then, the cable tension-time curve was transformed into the cable tension-deployment angle curve according to the predesigned motion for comparison with the results in Ref. [50].

Figure 7 shows the obtained cable tension. Figure 8 shows the deviation between the cable tensions obtained in this study and those reported in Ref. [50]. According to Figure 8, the maximum deviation was 1.1 N, which was less than 1.4% of the results. This demonstrates that the calculated cable tensions agree well with the results reported in Ref. [50], which verifies the accuracy of the calculation.

The comparison of the required driving force for the predesigned deployment motion is shown in Figure 9.

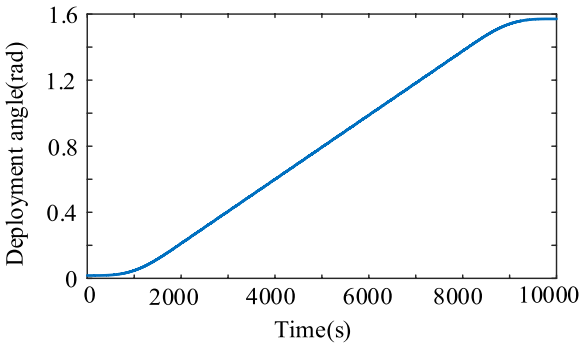

(a) Deployment angle

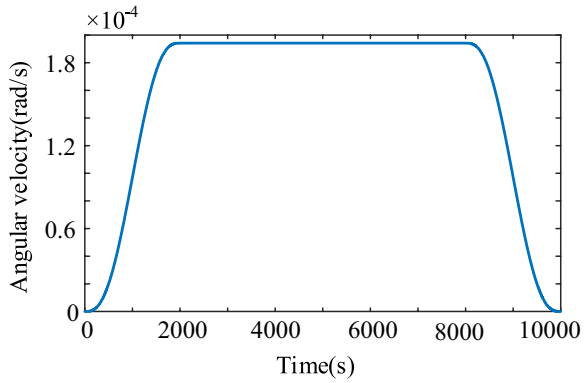

(b) Deployment angular velocity

Figure 6 Predesigned deployment motion [50]

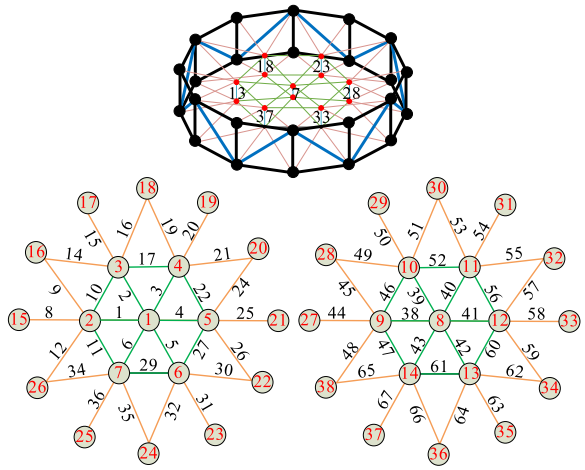

Figure 5 The cable network serial numbers of a mesh reflector antenna with twelve parallelogram units

Table 1 Parameters of the antenna with twelve parallelogram units

Parameter	Value
Length of transverse bar R_1(m)	1.242
Length of longitudinal bar R_2(m)	1.6
Mass of three-dimensional hinges m_t(kg)	0.3
Mass of five-dimensional hinges m_f(kg)	0.4
Mass of transverse bar m_1(kg)	0.131
Mass of longitudinal bar m_2(kg)	0.168
Mass of the oblique bar m_3(kg)	0.295
Tensile stiffness of cables k (N/mm)	15

Table 2 The cables' unstressed length (mm)

Location	Cables' number	Unstressed length
Front cable net	1~6	1201.81
	10, 11, 17, 22, 27, 29	1195.79
	8, 15, 20, 25, 31, 36	1254.97
	9, 12, 14, 16, 19, 21	1530.78
Rear cable net	24, 26, 30, 32, 34, 35	1201.81
	38~43	1195.79
	46, 47, 52, 56, 60, 61	1254.97
	44, 50, 54, 58, 63, 67	1530.78
Tension ties	45, 48, 49, 51, 53, 55	597.51
	57, 59, 62, 64, 65, 66	837.21

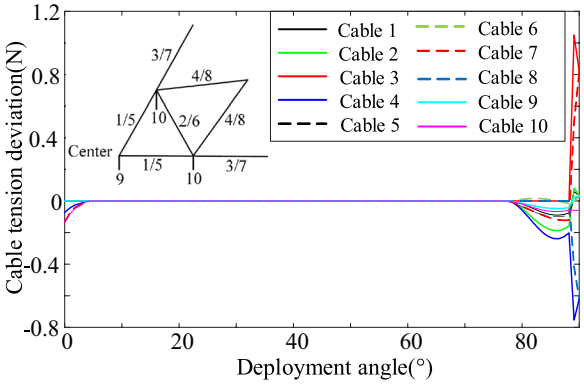

Figure 8 Deviation of the cable tensions

The maximum deviation is 24.2 N, which is less than 6.6% of the results in Ref. [60]. This indicates that the required driving force agree well with the previous literature, which verifies the accuracy of the proposed cable-truss coupling dynamic analysis method. As the calculation in Ref. [60] is based on the quasi-static analysis of the unfolding process of the cable network, and cable truss is decoupled in the modeling, it does not fully capture the coupling effects between the cable network and truss, leading to cable tension deviations.

In this study, numerical nonlinear and integral algorithms were used to solve the dynamic model. The numerical convergence and efficiency of the solution process were ensured by variable step size technology.

4.2 Experimental Verification

We made a scaled prototype of a ring-truss deployable antenna and designed an experimental system to verify the established deployment dynamic model. As shown in Figure 10, the prototype comprises six parallelogram-deployable units. The aperture is 0.75 m, height is 0.41 m, and the cable network contains 43 cables. A vertical rod was fixed on the frame, and a servomotor drove the roller to rotate and contract the driving rope along the diagonal line of the parallelogram. The driving force was transmitted by the diagonal rope to achieve the deployment of each unit. In the experiment, a constant driving force of 12 N was provided, the inertial measurement unit measured the acceleration of the truss node, and the measured data were transmitted wirelessly to the computer signal acquisition software for data processing.

The hinges and rods were made of resin and aluminum alloy tubes, respectively. Table 3 lists the truss parameters, while Figure 11 shows the cable network topology. Table 4 lists the original length of each cable.

Figure 12 shows the three states in the deployment process of the scaled prototype. The video of the entire deployment process and curves of the deployment angle, node displacement, and acceleration during the experiment are provided in the Supplementary Material.

The corresponding deployment angle was calculated using the proposed approach for comparison with the experimental results. The acceleration of the measuring point in Figure 11 was obtained, and the corresponding deployment angle was converted using Eq. (26), according to the geometric relationship shown in Figure 11. Gravity was considered in the simulation to maintain

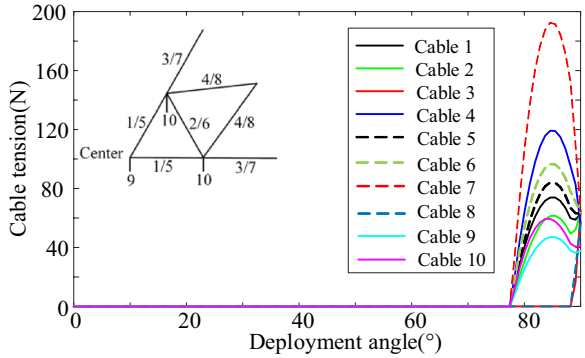

Figure 7 Cable tension-deployment angle curve

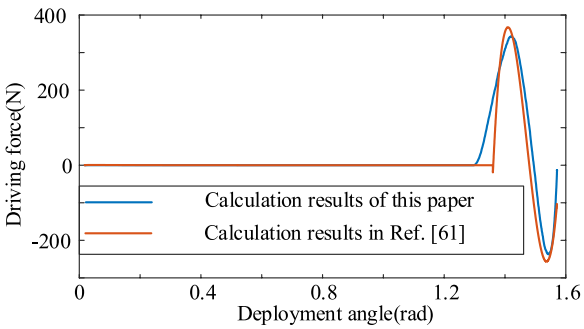

Figure 9 Comparison between the required driving force under the predesigned deployment motion

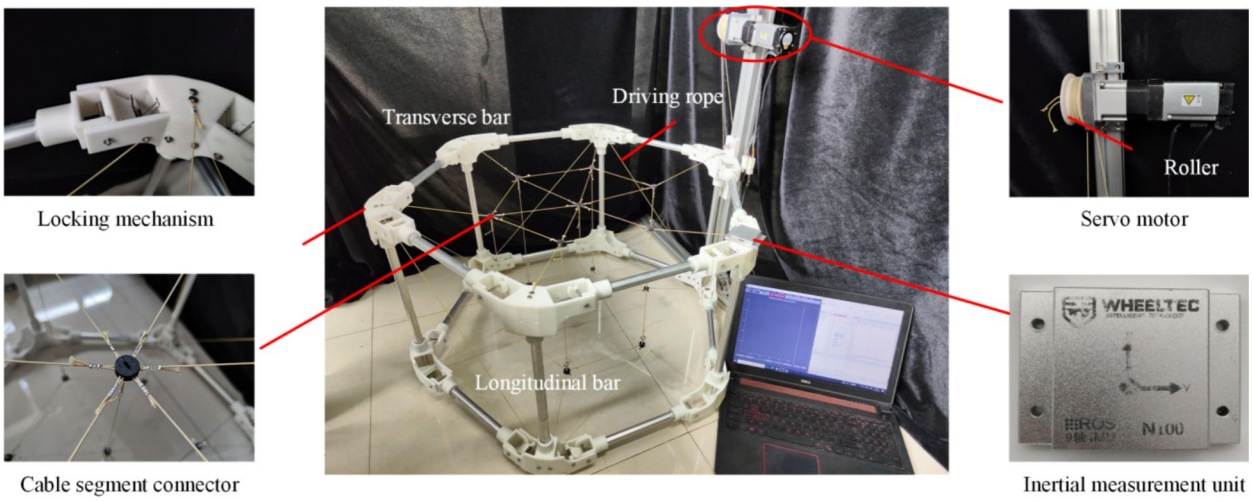

Figure 10 The prototype machine of the ring truss deployable antenna and test system

Table 3 Parameters of the antenna with twelve parallelogram units

Parameter	Symbol	Value	Unit
Length of transverse bar	R_1	0.3750	m
Length of longitudinal bar	R_2	0.4140	m
Mass of three-dimensional hinges	m_t	0.1639	kg
Mass of five-dimensional hinges	m_f	0.1804	kg
Mass of transverse bar	m_1	0.0204	kg
Mass of longitudinal bar	m_2	0.0225	kg

Table 4 The cables' unstressed length (mm)

Location	Cables' number	Unstressed length
Front cable net	1~6	188.3
	7~12	187.5
	13~18	194.8
Rear cable net	19~24	188.3
	25~30	187.5
	31~36	194.8
Tension ties	37	273.4
	38~43	308.5

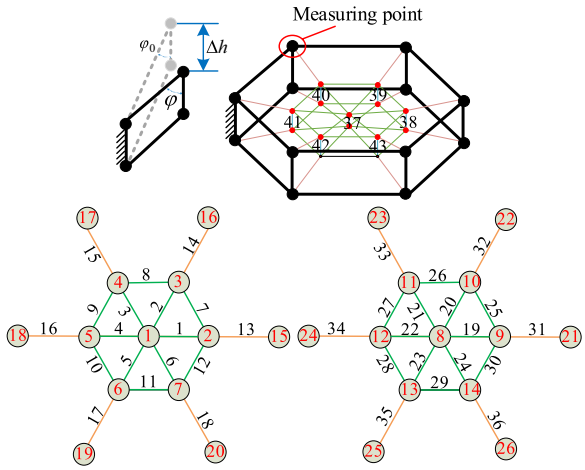

Figure 11 The cable network serial numbers of the prototype

consistency with the experiment without the gravity unloading device. As shown in Figure 13, oscillations occurred in the experimental curve owing to uncontrollable friction and motor vibration. However, the overall trend agreed well with the calculation results, verifying the correctness and accuracy of the proposed cable-truss coupled dynamic analysis method. The deployment angle varied slowly at the beginning and middle stages, and increased rapidly at the end of the stage. This is dependent on the antenna configuration. The acceleration at the end of deployment can be clearly observed in the video provided.

$$\begin{cases} \Delta h = \left| \iint a \mathrm{d}t \right|, \\ \varphi = \arccos\left(\dfrac{R_1 \cos\varphi_0 - \Delta h}{R_1} \right), \end{cases} \tag{26}$$

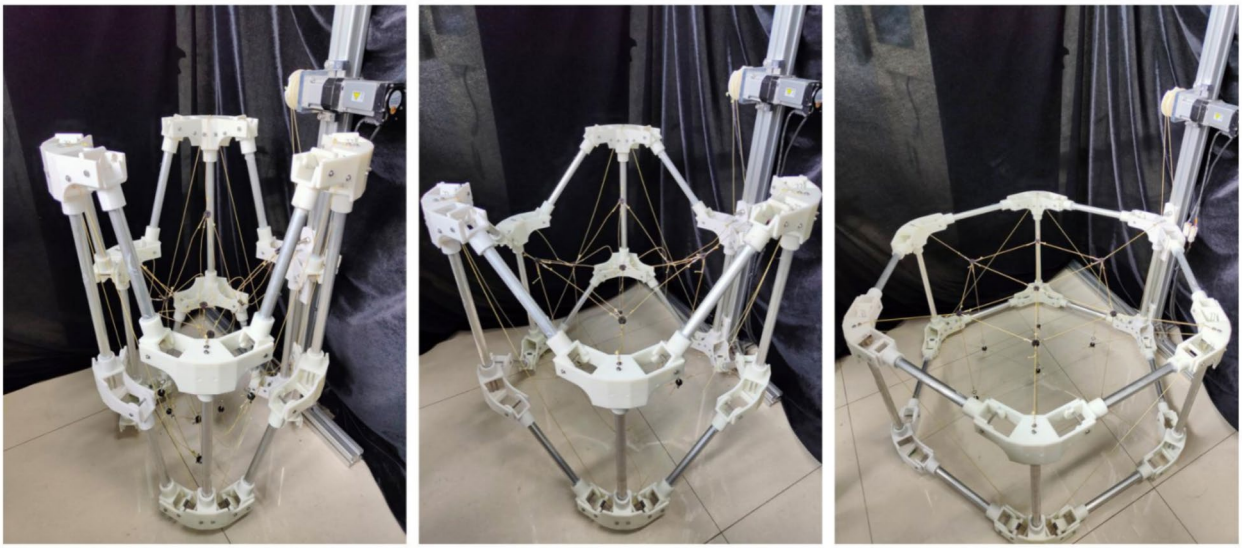

Figure 12 The deployment process of the scaled prototype

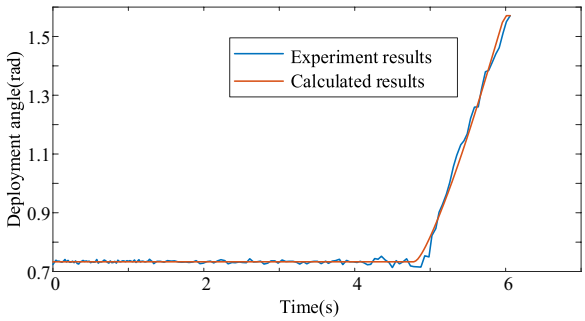

Figure 13 The deployment angle curves by the experiment and simulation

where a represents the acceleration of the measuring point; ϕ_0 is the initial value of the deployment angle; and R_1 is the length of the transverse bar.

5 Driving Scheme Design for the Ring Truss Deployable Antenna

Driving schemes significantly affect the deployment dynamic behavior. The real-time coupling effect between the soft cables and rigid truss makes the driving mode and parameter design more complex than the truss mechanism. This section introduces a driving scheme design method based on the proposed cable-truss coupled dynamic analysis model, discusses the characteristics of the rope and spring drives, and displays a series of numerical examples for the driving-scheme design.

5.1 Driving Schemes for the Ring Truss Deployable Antenna

Deployment can be regarded as a process in which the driving force or driving energy competes with the resistance load or energy. Figure 14 shows the variations in the driving and resistance forces and energies during deployment. Because the cable network is the main resistance load and most of the work done by the driving force/torque is converted into the elastic energy of the cable network, the elastic potential energy of the cable network is shown by the blue dotted curve in Figure 14. It is obtained by the approach in Ref. [50] and provides the basis for the driving scheme design.

The slope of the elastic energy curve at each deployment angle/driving rope length represents the resistance torque/force generated by the cable network at that state. If the driving force/torque is designed according to the maximum resistance force/torque (the maximum slope of the elastic energy curve), successful deployment can be achieved, but the deployment speed may be difficult to control. Nevertheless, if the driving force/torque is determined by the required energy, there is a risk of unsuccessful deployment, although the conservation-of-energy principle is satisfied. Therefore, the driving schemes based on the above design principles should be evaluated by the dynamic analysis in Section 3 and optimized based on the analysis results to ensure a smooth and successful deployment. The detailed driving scheme design is as follows. The antenna is driven by torsion springs in the initial deployment stage, and then deployed by driving rope. The design method proposed in this study can be used

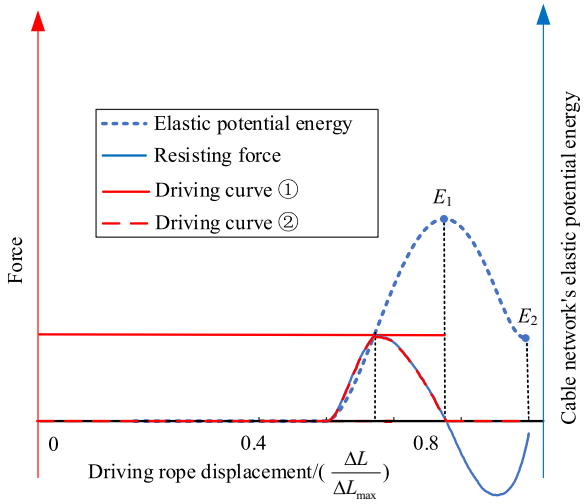

(a) Driving rope scheme

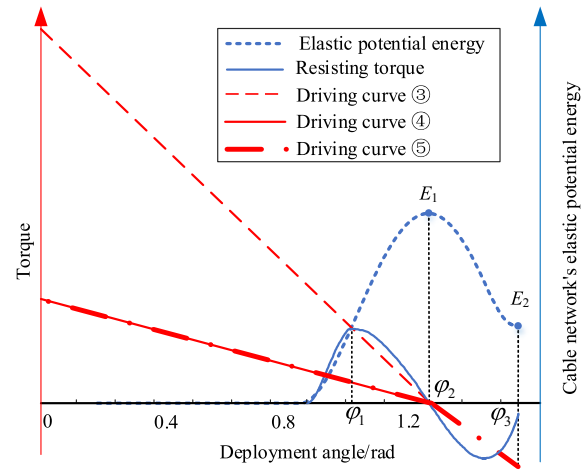

(b) Torsion-spring scheme

Figure 14 Schematic diagram for the driving schemes design

to design the driving torsion spring and rope to complete the actual engineering drive.

5.1.1 Driving Parameters Design for the Rope Drive

(1) The driving parameter design based on the required driving force. Constant-force driving is a simple and commonly used driving mode. If the constant driving force is provided by the driving rope, then the value of the constant force should not be less than the maximum resisting force, depicted by the blue curve in Figure 14(a), to ensure deployment success. The constant force provided by the driving rope can be calculated by Eq. (27), corresponding to the driving curve ① in Figure 14(a). A correction coefficient is added to the equation to offset the impact of system friction and damping on the deployment. The corresponding coefficients also need to be added to solve for the driving force in other driving schemes.

$$F_{\mathrm{rc}} = \alpha_1 \times \max\left(\frac{\partial E}{\partial L}\right), \tag{27}$$

where F_{rc} is the constant force provided by the driving rope; α_1 is the correction coefficient; E is the cable network's elastic potential energy; and L is the driving rope length.

(2) The driving parameter design based on the required energy. If the required energy in the deployment is taken as the basis for the driving-force calculation, the work done by the driving rope should be equal to the elastic energy of the cable network, kinetic energy of the truss, and the rest of the energy consumption. The driving force in the rope can be obtained by considering the derivative of the systematic total energy with respect to the length variation of the driving rope, as expressed in Eq. (28). It should be noted that the driving rope can only be tensioned and not compressed, and cannot provide a negative driving force. Thus, the calculated driving force corresponds to the driving curve ② in Figure 14(a).

$$F_{\mathrm{rv}} = \alpha_2 \times \max\left(\frac{\partial (E+T)}{\partial L}, 0\right), \tag{28}$$

where F_{rv} is the driving force provided by the driving rope, and α_2 is the correction coefficient.

5.1.2 Driving Parameters Design for the Torsion Spring Drive

(1) The driving parameter design based on the required driving force. Driving torsion springs are commonly arranged in five-dimensional hinges. In the folded state, the compression of the torsion spring was the largest, and then gradually decreased with deployment, accompanied by the decrease in the driving torque. To ensure a successful deployment, the driving torque at the arbitrary deployment angle should not be less than the maximum resisting torque at the corresponding deployment angle. In Figure 14(b), the maximum resisting torque occurs at the deployment angle ϕ_1 and the resisting torque equals 0 at the deployment angle ϕ_2, so the stiffness of the torsion spring can be determined by Eq. (29), which corresponds to the driving curve ③ in Figure 14 (b).

$$k_1 = \alpha_3 \times \frac{\max\left(\frac{\partial E}{\partial \varphi}\right)}{\varphi_2 - \varphi_1}, \tag{29}$$

where k_1 is the torsion spring stiffness; α_3 is the correction coefficient; ϕ_1 is the deployment angle corresponding to

the maximum slope of the cable network's elastic potential energy; and ϕ_2 is the deployment angle when the cable network's potential energy reaches the maximum value.

(2) The driving parameter design based on the required energy. The elastic potential energy stored in the torsion springs is converted into the kinetic energy of the truss and elastic energy of the cable network during deployment. As shown by the blue curve in Figure 14(b), the cable network's elastic potential energy reaches the maximum value at the deployment angle ϕ_2, so the torsion springs are required to expand the antenna before their deployment angle reaches ϕ_2. After that, the cable network's elastic potential energy begins to decrease, and the released elastic potential energy can provide the antenna's kinetic energy, which continues to drive the rest of the deployment process, as shown by the driving curve ④ in Figure 14(b), and the torsion spring stiffness is determined by Eq. (30).

$$k_2 = \alpha_4 \times \frac{2(E_1 + T_1)}{\varphi_2^2}, \tag{30}$$

where k_2 is the torsion spring's stiffness; α_4 is the correction coefficient; E_1 is the cable network's maximum elastic potential energy; and T_1 is the truss's kinetic energy when the deployment angle is equal to ϕ_2.

(3) The driving and braking torsion spring design based on the required energy. The braking spring stores energy as the antenna unfolds, in contrast to the driving spring, and its installation method is similar to that of the driving spring. As shown in Figure 14(b), the cable network's elastic energy increased before the deployment angle ϕ_1 and then decreased between the deployment angles ϕ_2 and ϕ_3. Correspondingly, the resisting torque is positive before the deployment angle ϕ_1 and then becomes negative between the deployment angle ϕ_2 and ϕ_3. To avoid the impact before locking, we attempt to deploy the antenna and reduce the deployment angular velocity at the final stage with two types of torsion springs: one type provides driving torque and the other provides braking torque. The stiffnesses of the driving and braking torsion springs were designed based on variations in the resistance load. The driving torsion spring has the same stiffness as the driving curve ④ (calculated by Eq. (30)), whereas the stiffness of the braking spring was determined by Eq. (31). The braking springs were used to absorb the released elastic energy and prevent all the released elastic energy from being transformed into the truss's kinetic energy, so as to effectively slow down the deployment, as shown by the driving curve ⑤ in Figure 14 (b).

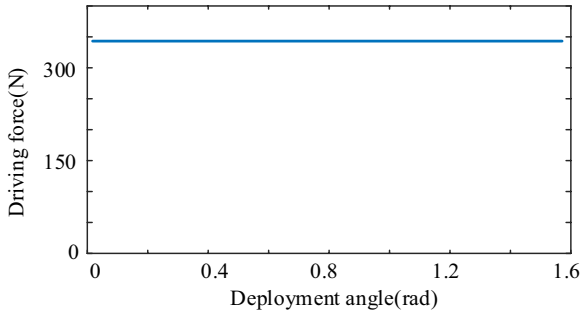

Figure 15 Constant force in the driving rope

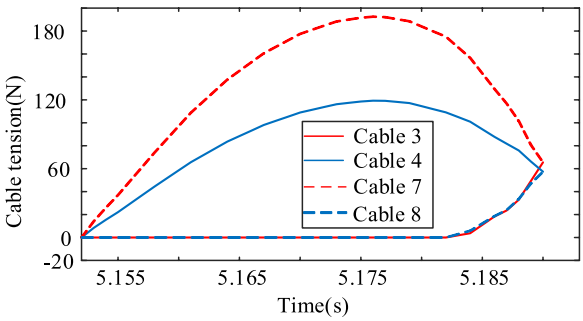

Figure 16 Boundary cables' time-varying tensions

$$k_3 = \alpha_5 \times \frac{2[(E_2 - E_1) + (T_2 - T_1)]}{(\varphi_3 - \varphi_2)^2}, \tag{31}$$

where k_3 is the braking spring's stiffness; α_5 is the correction coefficient; ϕ_3 is the deployment angle at the deployed state; E_2 is the cable network's elastic energy at the deployed state; and T_2 is the truss's kinetic energy at the deployed state.

5.2 Numerical Examples for Various Driving Schemes

This section provides several numerical examples to analyze the dynamic performance under different driving schemes. The time-varying tension of the boundary cable and the dynamic behaviors of the antenna under various driving parameters were analyzed to discuss their influence on the dynamic performance. The dissipative energy was used to simulate the loss caused by friction. The stiffness of the truss was neglected to improve the computational efficiency.

5.2.1 Deployment Dynamic Analysis Under the Rope Drive

(1) Dynamic simulation of the rope drive based on the required driving force (driving curve ① in Figure 14(a)).

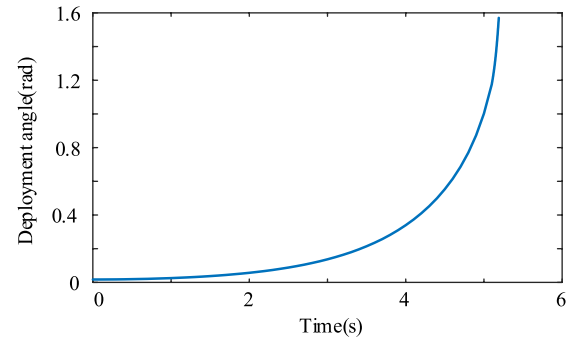

(a) Deployment Angle

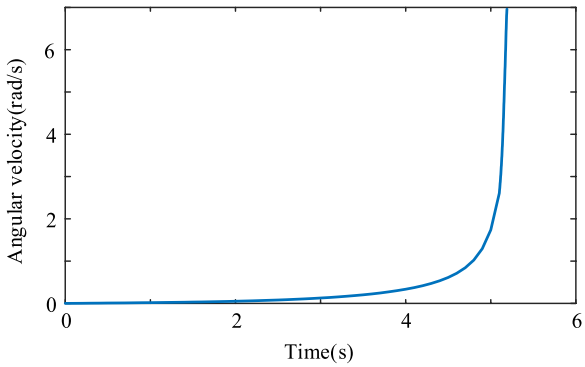

(b) Deployment angular velocity

Figure 17 Deployment motion under the constant driving force

In this section, we analyze the dynamic behavior of the antenna when the constant force determined by Eq. (27) is provided by the driving rope. Figure 15 shows the driving force.

Figure 16 shows the tension of the boundary cables, which are the main resistance load during deployment. Figure 17 shows the curves of the deployment angle and angular velocity under the constant driving force in Figure 15. It can be found that the deployment angular velocity increased throughout the entire process and increased sharply at the end of deployment, which was accompanied by the decreased tension of the boundary cables. The acceleration at the end of deployment may have a large impact before locking. Therefore, the simple constant-force drive is unsuitable for the desired smooth deployment pulled by the rope.

(2) Dynamic simulation of the rope drive based on the required energy (driving curve ② in Figure 14(a)).

In this section, we applied the driving force shown in Figure 18, which was determined by Eq. (28), to the same antenna to analyze the deployment motion under the rope drive.

Figure 19 shows the calculated time-varying tensions of the boundary cables, which are also the time-varying resistance load in the deployment. Figure 20 shows

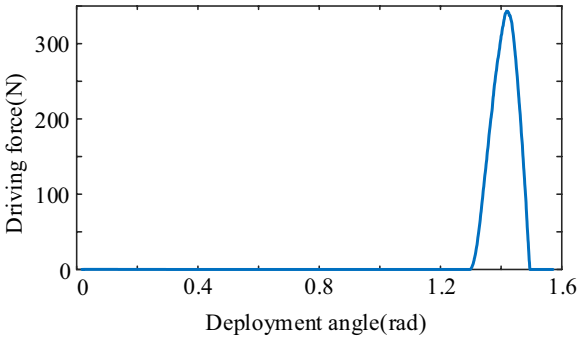

Figure 18 Driving force determined by the driving curve ② in Figure 14(a) and Eq. (28)

the calculated deployment angle and angular velocity under the driving force in Figure 18. It can be found that the antenna's motion is smooth in the early and middle stages, which is highly consistent with the predesigned deployment motion shown in Figure 6. The angular velocity increased sharply at 8574 s, which was caused by the release of the elastic potential energy of the cable network and the feature that the rope drive could not provide a braking force. Therefore, the rope drive may lead to a significant impact before locking.

5.2.2 Deployment Dynamic Analysis Under the Torsion Spring Drive

(1) Dynamic simulation of torsion spring drive based on the required driving force (driving curve ③ in Figure 14(b)).

The torsion-spring driving parameters are calculated according to Eq. (29). The calculated driving torque is shown in Figure 21.

The boundary cable tension, deployment angle, and angular velocity under the torsion-spring driving torque in Figure 21 were calculated by the proposed dynamic approach. The results are shown in Figures 22 and 23. The driving torque of the torsion springs decreased gradually with the increase in the deployment angle owing

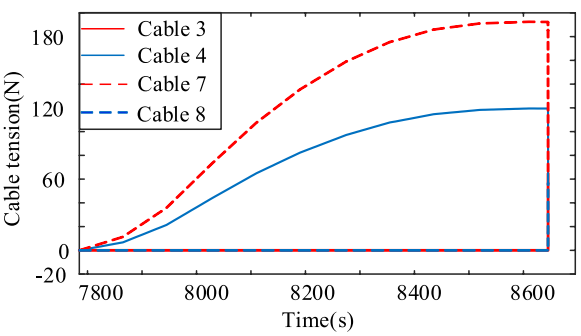

Figure 19 Boundary cables' time-varying tensions

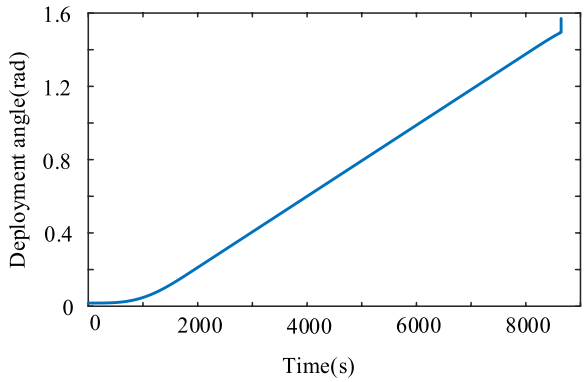

(a) Deployment Angle

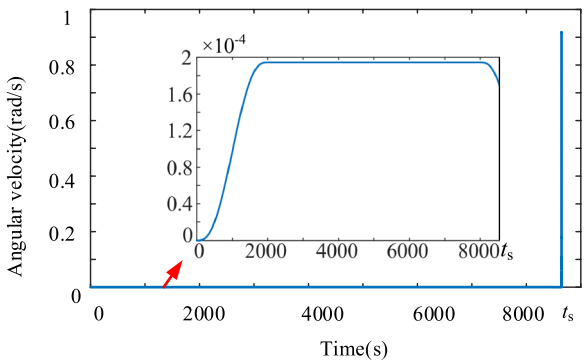

(b) Deployment angular velocity

Figure 20 Deployment motion under the driving force in Figure 18

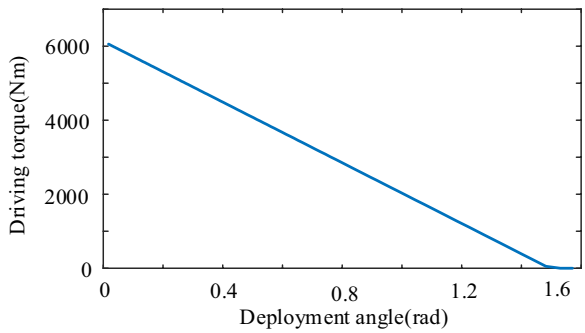

Figure 21 The driving torque-deployment angle curve for the torsion springs

to the characteristics of the torsion spring drive. However, the required maximum driving torque occurred in the late stage. Therefore, the driving torque provided by the torsion spring must be designed to be far more than that required in the early and middle stages to meet the requirement at the late stage, leading to a quick deployment, as shown in Figure 23.

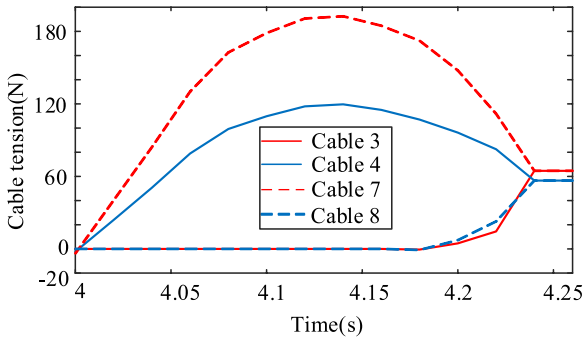

Figure 22 Boundary cables' time-varying tensions

(2) Dynamic simulation of torsion spring drive based on the required energy (driving curve ④ in Figure 14(b)).

The driving torque-deployment angle curve for the torsion springs is calculated by Eq. (30), as shown in Figure 24.

We conducted the deployment dynamic analysis for the mesh reflector antenna driven by the torsion spring with the stiffness shown in Figure 24. The calculated boundary cable tension, deployment angle curve, and deployment angular velocity curves are shown in Figures 25 and 26.

According to the torsion spring characteristics, the driving torque gradually decreased with an increase in the deployment angle. However, the main resistance of the antenna during deployment, provided by the boundary cables, occurred at the final stage. This means that the residual torque of the torsion spring should be sufficiently large to cover the maximum resistance load of the cable network at the end of the deployment, which leads to a waste of driving energy in the early and middle stages. As shown in Figure 26, the driving torque of the torsion spring was sufficiently large to deploy the truss before time t_1, and the resistance of the boundary cables was very small, as shown in Figure 25. Therefore, the deployment angle and angular velocity increased rapidly before time t_1. Subsequently, the resistance of the boundary cables increased, and the driving torque was less than the required torque, which led to a decrease in the deployment velocity, as shown in Figure 26(b). The boundary cable resistance increased within times t_1 and t_2, which correspond to the slow increase in the deployment angle in Figure 26(a) and the rapid decrease in the deployment angular velocity in Figure 26(b). The torque of the torsion spring was set to zero at the deployment angle where the cable network's elastic potential energy reached the maximum value to save energy and slow down deployment. However, after time t_2, the resistance of the boundary cables began to decrease, and the deployment velocity increased correspondingly, as

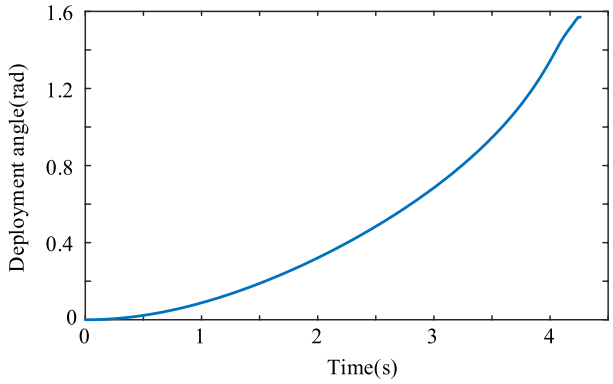

(a) Deployment angle (b) Deployment angular velocity

Figure 23 Deployment motion under the torsion spring drive

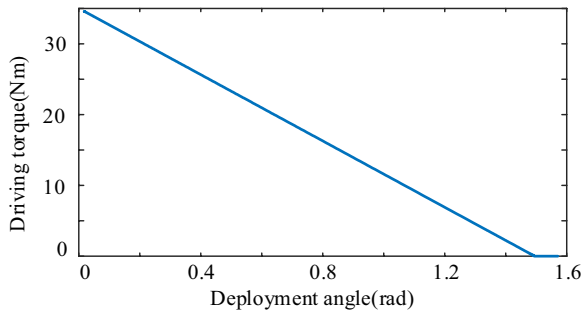

Figure 24 The designed driving torque-deployment angle curve for the torsion springs

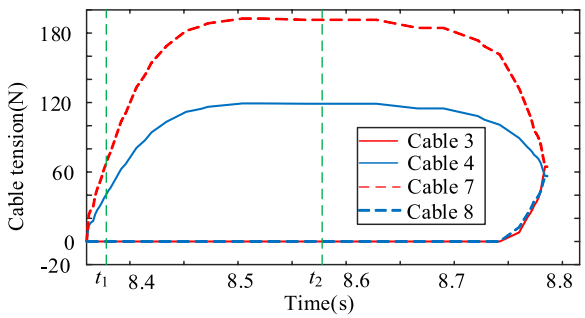

Figure 25 Boundary cables' time-varying tensions

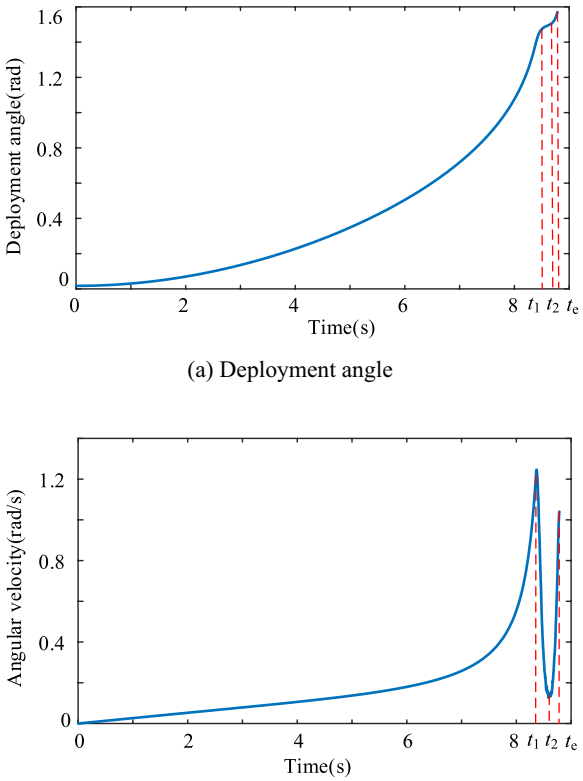

(a) Deployment angle

(b) Deployment angular velocity

Figure 26 Deployment motion under the torsion spring drive

shown in Figure 26(b). Most importantly, the antenna deployment velocity in the later stages is relatively high, which may lead to a large impact before locking.

(3) Dynamic simulation under the driving and braking torsion spring drive based on the required energy (driving curve ⑤ in Figure 14(b)).

Based on the stiffness values calculated using Eq. (31), the driving torque-deployment curve of the braking spring was obtained, as shown in Figure 27. The curve before the deployment angle ϕ_2 represents the driving torque of the driving spring, while the curve between the deployment angle ϕ_2 and ϕ_3 represents the braking torque of the braking spring.

The boundary cable tension, deployment angle, and angular velocity under the torsion spring drive with driving torque in Figure 27 were calculated by the

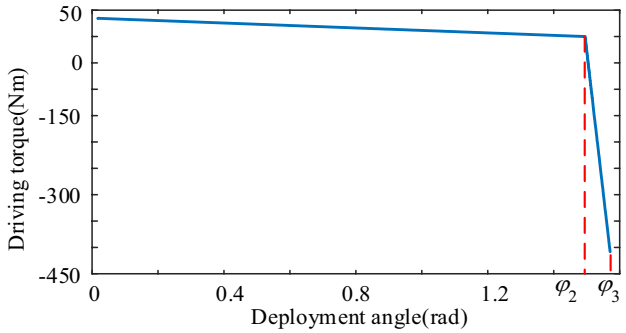

Figure 27 Driving torque provided by the driving and braking torsion springs

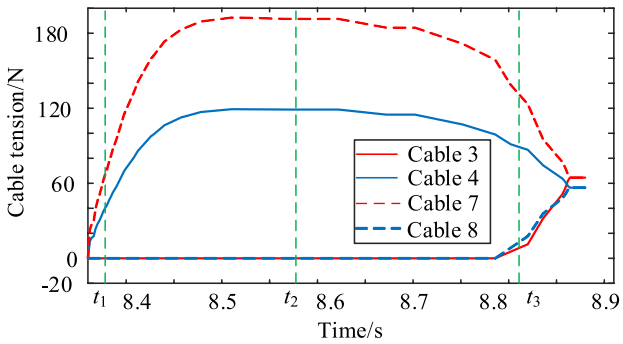

Figure 28 Boundary cables' time-varying tensions

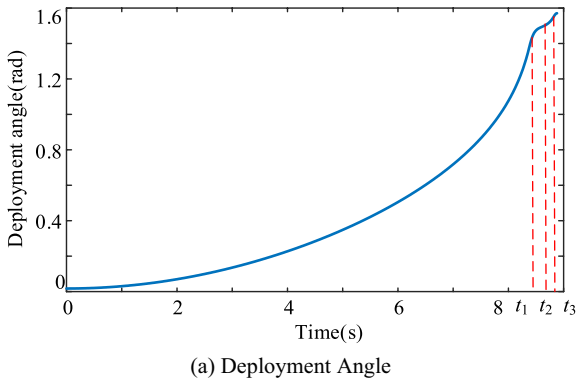

(a) Deployment Angle

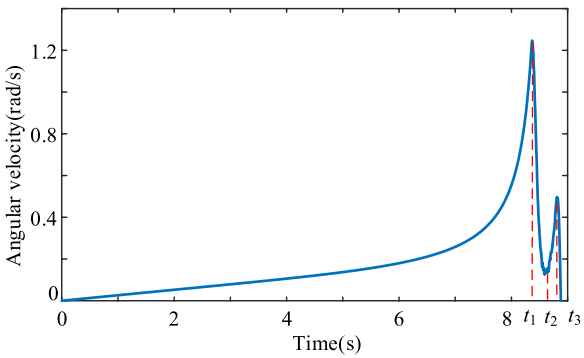

(b) Deployment angular velocity

Figure 29 Deployment motion under the driving and braking torsion springs

proposed dynamic method. The results are shown in Figures 28 and 29. As the braking spring began to act at time t_2, the variations in the deployment angle and deployment angular velocity before time t_2 in Figure 29 were the same as those in the curves in Figure 26. Because the braking torque was initially small, the deployment angular velocity of the antenna continued to increase within time t_2 and t_3. Then, the braking springs' torque balances the released elastic energy of the cable network at time t_3, and the antenna deployment angular velocity started to decrease from time t_3 until the fully deployed moment, and finally reached zero. Obviously, the braking torsion springs can significantly slow down the deployment at the final stage, which avoids the impact before locking.

6 Conclusions

(1) This study proposed a general cable-truss coupling dynamic analysis methodology for cable antennas, which provides an effective tool for analyzing and improving the deployment dynamic behaviors of cable antennas with varying topologies and parameters.

(2) We derived the explicit expression of the time-varying resistance provided by the boundary cables, which helped achieve real-time coupling between the soft cables and truss. The topological diversity, geometric nonlinearity, and continuous switching between the slacked and tensioned states of the cable network were fully captured during modeling.

(3) A scaled prototype was fabricated, and a deployment experiment was conducted to verify the accu-

racy of the proposed cable-truss coupled dynamic analysis method.

(4) The effects of the driving modes and parameters on the dynamic performance were well studied, and the driving scheme design, including the rope drive and torsion spring drive for a cable–mesh antenna, were displayed.

(5) The uncontrollable acceleration at the end of deployment caused by the cable network's features was effectively overcome by adding the braking torsion springs, which avoided the commonly occurring impact of cable antennas caused by the cable network's elastic energy release before locking.

Acknowledgements
Not applicable.

Author Contributions
BH performed the conceptualization, funding acquisition, resources, and supervision. LJ conducted the methodology, data curation, formal analysis, and software development. KL performed data curation, formal analysis, software development, and writing of the original draft. RN conducted the investigation and supervised, validated, wrote, reviewed, and edited the manuscript. YF supervised and visualized the data. GW performed the project administration and supervision. All the authors have read and approved the final version of the manuscript.

Funding
Supported by National Key R&D Program of China (Grant No. 2023YFB3407103), National Natural Science Foundation of China (Grant Nos. 52175242, 52175027), and Young Elite Scientists Sponsorship Program by CAST (Grant No. 2022QNRC001).

Availability of Data and Materials
The datasets used and/or analyzed in the current study are available from the corresponding author upon reasonable request.

Declarations

Competing Interests
The authors declare no competing financial interests.

Received: 22 March 2024 Revised: 24 June 2024 Accepted: 27 June 2024
Published online: 26 July 2024

References

[1] Z Sun, Y Zhang, D Yang, et al. Structural design, analysis, and experimental verification of an H-style deployable mechanism for large space-borne mesh antennas. *Acta Astronautica*, 2021, 178: 481-498. https://doi.org/https://doi.org/10.1016/j.actaastro.2020.09.032.

[2] B Han, Y Xu, J Yao, et al. Design and analysis of a scissors double-ring truss deployable mechanism for space antennas. *Aerospace Science and Technology*, 2019, 93: 105357. https://doi.org/https://doi.org/10.1016/j.ast.2019.105357.

[3] Z Sun, D Yang, B Duan, et al. Structural design, dynamic analysis, and verification test of a novel double-ring deployable truss for mesh antennas. *Mechanism and Machine Theory*, 2021, 165: 104416. https://doi.org/https://doi.org/10.1016/j.mechmachtheory.2021.104416.

[4] W Cao, S Xi, H Ding, et al. Design and kinematics of a novel double-ring truss deployable antenna mechanism. *Journal of Mechanical Design*, 2021, 143(12): 124502. https://doi.org/https://doi.org/10.1115/1.4051352.

[5] Y Zhang, D Yang, Z Sun, et al. Winding strategy of driving cable based on dynamic analysis of deployment for deployable antennas. *Journal of Mechanical Science and Technology*, 2019, 33(11): 5147-5156. https://doi.org/https://doi.org/10.1007/s12206-019-0906-9.

[6] X Qi, H Huang, B Li, et al. A large ring deployable mechanism for space satellite antenna. *Aerospace Science and Technology*, 2016, 58: 498-510. https://doi.org/https://doi.org/10.1016/j.ast.2016.09.014.

[7] J Guo, Y Zhao, Y Xu, et al. Design and analysis of truss deployable antenna mechanism based on a novel symmetric hexagonal profile division method. *Chinese Journal of Aeronautics*, 2021, 34(8): 87-100. https://doi.org/https://doi.org/10.1016/j.cja.2020.06.004.

[8] H Yang, S Fan, Y Wang, et al. Novel four-cell lenticular honeycomb deployable boom with enhanced stiffness. *Materials*, 2022, 15(1): 306. https://doi.org/https://doi.org/10.3390/ma15010306.

[9] J Shore, A Viquerat, G Richardson, et al. Rotational stiffness of drum deployed thin-walled open tubular booms. *Thin-Walled Structures*, 2020, 150: 106704. https://doi.org/https://doi.org/10.1016/j.tws.2020.106704.

[10] B Han, D Zheng, Y Xu, et al. Kinematic characteristics and dynamics analysis of an overconstrained scissors double-hoop truss deployable antenna mechanism based on screw theory. *IEEE Access*, 2019, 7: 140755-140768. https://doi.org/https://doi.org/10.1109/ACCESS.2019.2930101.

[11] M W Thomson. The AstroMesh deployable reflector. *IEEE Antennas and Propagation Society International Symposium*. 1999 Digest. Held in conjunction with: USNC/URSI National Radio Science Meeting (Cat. No.99CH37010): 3. Orlando, FL, USA: IEEE, 1999: 1516-1519[2023-12-25]. http://ieeexplore.ieee.org/document/838231/.

[12] P F Yuan, B Y He, L H Zhang, et al. Topology generation and optimization of boundary cable nets for the mesh reflector antenna. *Engineering Structures*, 2021, 229: 111630. https://doi.org/https://doi.org/10.1016/j.engstruct.2020.111630.

[13] R Nie, B Y He, S Yan, et al. Design optimization of mesh antennas for on-orbit thermal effects. *International Journal of Mechanical Sciences*, 2020, 175: 105547. https://doi.org/https://doi.org/10.1016/j.ijmecsci.2020.105547.

[14] Y Zhang, N Li, G Yang, et al. Dynamic analysis of the deployment for mesh reflector deployable antennas with the cable-net structure. *Acta Astronautica*, 2017, 131: 182-189. https://doi.org/https://doi.org/10.1016/j.actaastro.2016.11.038.

[15] P F Yuan, B Y He, L H Zhang, et al. Pretension design for mesh reflector antennas with flexible trusses and hinges based on the equilibrium matrix method. *Aerospace Science and Technology*, 2023, 140: 108437. https://doi.org/https://doi.org/10.1016/j.ast.2023.108437.

[16] S Zhang, S Zhang, Y Gu, et al. Thermal design optimization method of mesh reflector antennas considering the interaction between cable net and flexible truss. *Structural and Multidisciplinary Optimization*, 2023, 66(4): 68. https://doi.org/https://doi.org/10.1007/s00158-023-03527-7.

[17] G Yang, A Tang, Z Yuan, et al. Surface shape stability design of mesh reflector antennas considering space thermal effects. *IEEE Access*, 2020, 8: 89071-89083. https://doi.org/https://doi.org/10.1109/ACCESS.2020.2993813.

[18] Z Ren, J Du, H Bao, et al. Shape adjustment for uncertain mesh reflectors using machine learning. *International Journal of Mechanical Sciences*, 2023, 244: 108082. https://doi.org/https://doi.org/10.1016/j.ijmecsci.2022.108082.

[19] J Zhang, B Y He, L H Zhang, et al. High surface accuracy and pretension design for mesh antennas based on dynamic relaxation method. *International Journal of Mechanical Sciences*, 2021, 209: 106687. https://doi.org/https://doi.org/10.1016/j.ijmecsci.2021.106687.

[20] B Y He, K K Li, R Nie, et al. Deployment modeling for soft cable networks from slack to tension. *International Journal of Mechanical Sciences*, 2022, 221: 107225. https://doi.org/https://doi.org/10.1016/j.ijmecsci.2022.107225.

[21] F Zheng, M Chen. New conceptual structure design for affordable space large deployable antenna. *IEEE Transactions on Antennas and Propagation*, 2015, 63(4): 1351-1358. https://doi.org/https://doi.org/10.1109/TAP.2015.2404345.

[22] M Mobrem, S Kuehn, C Spier, et al. Design and performance of Astromesh reflector onboard Soil Moisture Active Passive spacecraft//*2012 IEEE*

Aerospace Conference. Big Sky, MT: IEEE, 2012: 1-10[2023-12-25]. http://ieeexplore.ieee.org/document/6187094/.
[23] G Yang, Y Zhang, A Tang, et al. A design approach for Astromesh-type contoured-beam reflector antennas. *IEEE Antennas and Wireless Propagation Letters*, 2018, 17(6): 951-955. https://doi.org/https://doi.org/10.1109/LAWP.2018.2825475.
[24] Y Zhang, Z Sun, D Yang, et al. Performance coordination of structure and deployment properties of deployable antenna. *Journal of Aerospace Engineering*, 2019, 32(5): 04019073. https://doi.org/https://doi.org/10.1061/(ASCE)AS.1943-5525.0001069.
[25] Y Zhang, B Duan, T Li. A controlled deployment method for flexible deployable space antennas. *Acta Astronautica*, 2012, 81(1): 19-29. https://doi.org/https://doi.org/10.1016/j.actaastro.2012.05.033.
[26] W Guo, Y Li, Y Z Li, et al. Thermal–structural analysis of large deployable space antenna under extreme heat loads. *Journal of Thermal Stresses*, 2016, 39(8): 887-905. https://doi.org/https://doi.org/10.1080/01495739.2016.1189776.
[27] X Y Wu, A P Luo. Asynchronous phenomenon of the ring truss deployable antenna. *Applied Mechanics and Materials*, 2012, 170-173: 3415-3418. https://doi.org/https://doi.org/10.4028/www.scientific.net/AMM.170-173.3415.
[28] J Zhao, J Yang, Y Xiao, et al. Deployment strategy and dynamic analysis of large ring truss antenna. *International Journal of Aerospace Engineering*, 2022, 2022: 1-9. https://doi.org/https://doi.org/10.1155/2022/4725423.
[29] R W Gehle, S F Masri. Active control of shallow, slack cable using the parametric control of end tension. *Nonlinear Dynamics*, 1998, 17(1): 77-94. https://doi.org/https://doi.org/10.1023/A:1008212828873.
[30] Y Xu, F Guan, X Xu, et al. Development of a novel double-ring deployable mesh antenna. *International Journal of Antennas and Propagation*, 2012: 1-10. https://doi.org/10.1155/2012/375463.
[31] X Du, J Du, H Bao, et al. Dynamic analysis of the deployment for mesh reflector antennas driven with variable length cables. *Journal of Computational and Nonlinear Dynamics*, 2019, 14(11): 111006. https://doi.org/https://doi.org/10.1115/1.4044315.
[32] Y Zhang, Q Feng, G Wang, et al. Analytical model for the bending of parallel wire cables considering interactions among wires. *International Journal of Mechanical Sciences*, 2021, 194: 106192. https://doi.org/https://doi.org/10.1016/j.ijmecsci.2020.106192.
[33] Z Chu, Z Deng, X Qi, et al. Modeling and analysis of a large deployable antenna structure. *Acta Astronautica*, 2014, 95: 51-60. https://doi.org/https://doi.org/10.1016/j.actaastro.2013.10.015.
[34] R Q Feng, J Ye, G Yan, et al. Dynamic nonlinearity and nonlinear single-degree-of-freedom model for cable net glazing. *Journal of Engineering Mechanics*, 2013, 139(10): 1446-1459. https://doi.org/https://doi.org/10.1061/(ASCE)EM.1943-7889.0000575.
[35] M H Wei, K Lin, L Jin, et al. Nonlinear dynamics of a cable-stayed beam driven by sub-harmonic and principal parametric resonance. *International Journal of Mechanical Sciences*, 2016, 110: 78-93. https://doi.org/https://doi.org/10.1016/j.ijmecsci.2016.03.007.
[36] A Arena, A Pacitti, W Lacarbonara. Nonlinear response of elastic cables with flexural-torsional stiffness. *International Journal of Solids and Structures*, 2016, 87: 267-277. https://doi.org/https://doi.org/10.1016/j.ijsolstr.2015.09.019.
[37] S Yuan, W Zhu. A Cartesian spatial discretization method for nonlinear dynamic modeling and vibration analysis of tensegrity structures. *International Journal of Solids and Structures*, 2023, 270: 112179. https://doi.org/https://doi.org/10.1016/j.ijsolstr.2023.112179.
[38] H Jianfeng, W Lipeng, Y Jungang. The pretension design of cable mesh considering the large deformation of ring truss. *International Journal of Aerospace Engineering*, 2023: 1-9. https://doi.org/10.1155/2023/1282797.
[39] D L Msongaleli, F Dikbiyik, M Zukerman, et al. Disaster-aware submarine fiber-optic cable deployment//2015 *International Conference on Optical Network Design and Modeling (ONDM)*. Pisa, Italy: IEEE, 2015: 245-250[2023-12-25]. http://ieeexplore.ieee.org/document/7127306/.
[40] K Fu, Z Zhao, G Ren, et al. From multiscale modeling to design of synchronization mechanisms in mesh antennas. *Acta Astronautica*, 2019, 159: 156-165. https://doi.org/https://doi.org/10.1016/j.actaastro.2019.03.056.
[41] S Yuan, B Yang. The fixed nodal position method for form finding of high-precision lightweight truss structures. *International Journal of Solids and Structures*, 2019, 161: 82-95. https://doi.org/https://doi.org/10.1016/j.ijsolstr.2018.11.011.
[42] S Morterolle, B Maurin, J Quirant, et al. Numerical form-finding of geotensoid tension truss for mesh reflector. *Acta Astronautica*, 2012, 76: 154-163. https://doi.org/https://doi.org/10.1016/j.actaastro.2012.02.025.
[43] S Yuan, W Jing. Optimal shape adjustment of large high-precision cable network structures. *AIAA Journal*, 2021, 59(4): 1441-1456. https://doi.org/https://doi.org/10.2514/1.J059989.
[44] T S Walton, H Polachek. Calculation of transient motion of submerged cables. *Mathematics of Computation*, 1960, 14(69): 27-46. https://doi.org/https://doi.org/10.1090/S0025-5718-1960-0116470-5.
[45] X Sun, Y Yin, Y Jin, et al. The modeling of single-boat, mid-water trawl systems for fishing simulation. *Fisheries Research*, 2011, 109(1): 7-15. https://doi.org/https://doi.org/10.1016/j.fishres.2010.12.027.
[46] Ji Oh Song, E J Haug. Dynamic analysis of planar flexible mechanisms. *Computer Methods in Applied Mechanics and Engineering*, 1980, 24(3): 359-381. https://doi.org/10.1016/0045-7825(80)90070-5.
[47] J Xu, J Jia. Study on dynamics, stability and control of multi-body flexible structure system in functional space. *Applied Mathematics and Mechanics*, 2001, 22(12): 1410-1421. https://doi.org/https://doi.org/10.1023/A:1022834810297.
[48] Y L Hwang, V T Truong. Dynamic analysis and control of multi-body manufacturing systems based on Newton–Euler formulation. *International Journal of Computational Methods*, 2015, 12(2): 1550007. https://doi.org/https://doi.org/10.1142/S0219876215500073.
[49] L Greco, N Impollonia, M Cuomo. A procedure for the static analysis of cable structures following elastic catenary theory. *International Journal of Solids and Structures*, 2014, 51(7-8): 1521-1533. https://doi.org/https://doi.org/10.1016/j.ijsolstr.2014.01.001.
[50] R Nie, B Y He, L H Zhang, et al. Deployment analysis for space cable net structures with varying topologies and parameters. *Aerospace Science and Technology*, 2017, 68: 1-10. https://doi.org/https://doi.org/10.1016/j.ast.2017.05.008.
[51] J Ambrósio, M Neto, R Leal. Optimization of a satellite with composite materials. *Journal of Mechanics of Materials and Structures*, 2007, 2(8): 1397-1419. https://doi.org/https://doi.org/10.2140/jomms.2007.2.1397.
[52] L Dai, R Xiao. Optimal design and analysis of deployable antenna truss structure based on dynamic characteristics restraints. *Aerospace Science and Technology*, 2020, 106: 106086. https://doi.org/https://doi.org/10.1016/j.ast.2020.106086.
[53] B Siriguleng, W Zhang, T Liu, et al. Vibration modal experiments and modal interactions of a large space deployable antenna with carbon fiber material and ring-truss structure. *Engineering Structures*, 2020, 207: 109932. https://doi.org/https://doi.org/10.1016/j.engstruct.2019.109932.
[54] W Zhang, R Q Wu, K Behdinan, et al. Nonlinear dynamic analysis near resonance of a beam-ring structure for modeling circular truss antenna under time-dependent thermal excitation. *Aerospace Science and Technology*, 2019, 86: 296-311. https://doi.org/https://doi.org/10.1016/j.ast.2019.01.018.
[55] Y Cui, P Lan, H Zhou, et al. The rigid-flexible-thermal coupled analysis for spacecraft carrying large-aperture paraboloid antenna. *Journal of Computational and Nonlinear Dynamics*, 2020, 15(3): 031003. https://doi.org/https://doi.org/10.1115/1.4045890.
[56] M Liu, D Cao, D Zhu. Equivalent dynamic model of the space antenna truss with initial stress. *AIAA Journal*, 2020, 58(4): 1851-1863. https://doi.org/https://doi.org/10.2514/1.J058647.
[57] Y Zhang, D Yang, S Li. An integrated control and structural design approach for mesh reflector deployable space antennas. *Mechatronics*, 2016, 35: 71-81. https://doi.org/https://doi.org/10.1016/j.mechatronics.2015.12.009.
[58] S Lu, X Qi, Y Hu, et al. Deployment dynamics of large space antenna and supporting arms. *IEEE Access*, 2019, 7: 69922-69935. https://doi.org/https://doi.org/10.1109/ACCESS.2019.2918614.
[59] X Jiang, Z Bai. Dynamics modelling and simulation for deployment characteristics of mesh reflector antennas. *Applied Sciences*, 2020, 10(21): 7884. https://doi.org/https://doi.org/10.3390/app10217884.
[60] R Nie, B Y He, L H Zhang. Deployment dynamics modeling and analysis for mesh reflector antennas considering the motion feasibility. *Nonlinear Dynamics*, 2018, 91(1): 549-564. https://doi.org/https://doi.org/10.1007/s11071-017-3891-5.
[61] Q Meng, X J Liu, F Xie. Structure design and kinematic analysis of a class of ring truss deployable mechanisms for satellite antennas

based on novel basic units. *Mechanism and Machine Theory*, 2022, 174: 104881. https://doi.org/https://doi.org/10.1016/j.mechmachtheory.2022.104881.
[62] R Q Wu, W Zhang, J E Chen, et al. Dynamic modeling and analytical global mode shapes of a folded beam-ring structure for a truss antenna reflector with two arms. *Applied Mathematical Modelling*, 2022, 110: 542-561. https://doi.org/https://doi.org/10.1016/j.apm.2022.06.015.
[63] X K Wang, B Cai, H F Fang, et al. Deployment analysis of a deployable truss structure://*International Conference on Computer Information Systems and Industrial Applications*. Bangkok, Thailand, 2015[2024-01-10]. https://www.atlantis-press.com/article/22702.
[64] M Liu, D Cao, D Zhu. Coupled vibration analysis for equivalent dynamic model of the space antenna truss. *Applied Mathematical Modelling*, 2021, 89: 285-298. https://doi.org/https://doi.org/10.1016/j.apm.2020.07.013.

Baiyan He born in 1973, is currently a Professor at the *Key Laboratory of Mechanism Theory and Equipment Design of Ministry of Education, Tianjin University, China*. He received his Ph.D. from *Tianjin University, China*, in 2003. His research interests include the dynamics and control of mechanical multibody systems.

Lijun Jia born in 1998, is currently a master's candidate at the *Key Laboratory of Mechanism Theory and Equipment Design of Ministry of Education, Tianjin University, China*.

Kangkang Li born in 1995, is currently a Ph.D. candidate at the *Key Laboratory of Mechanism Theory and Equipment Design of Ministry of Education, Tianjin University, China*.

Rui Nie born in 1990, is currently an Associate Professor at the Key Laboratory of Mechanism Theory and Equipment Design of Ministry of Education, Tianjin University, China. She received her Ph.D. from Tianjin University, China, in 2018. Her research interests include deployable structures and multi-body dynamics.

Yesen Fan born in 1977, is currently a Professor at the *Xi'an Institute of Space Radio Technology, China*. He received his Ph.D. from *Northwestern Polytechnical University, China*, in 2011. His research interests include deployable antennas.

Guobiao Wang born in 1964, is currently a professor at the *Key Laboratory of Mechanism Theory and Equipment Design of Ministry of Education, Tianjin University, China*. He received his Ph.D. degree from *China University of Mining and Technology, China*, in 1992. His research interests include modern design and optimization design of machinery.